Reconstruction of Subsurface Objects by LSM and FWI From Limited-Aperture Electromagnetic Data

Miao Zhong, Yanjin Chen, Jiawen Li, and Feng Han, *Senior Member, IEEE*

***Abstract*— This article presents a hybrid 3-D electromagnetic (EM) full-wave inversion (FWI) method for the reconstruction of subsurface objects illuminated by an antenna array with the limited aperture. The 3-D linear sampling method (LSM) is first used to qualitatively reconstruct the rough shapes and locations of the subsurface objects. Then, the 3-D convolutional neural network (CNN) U-Net is used to further refine the images of the unknown objects. Finally, the Born iterative method (BIM) is implemented to quantitatively invert for the dielectric parameters of subsurface inhomogeneous objects or multiple homogeneous objects in the restricted image regions. Numerical simulations show that, compared with the pure FWI method BIM, the proposed hybrid method can reconstruct subsurface 3-D objects from limited-aperture EM data with both higher accuracy and lower computational cost. In addition, the proposed hybrid method also shows a strong antinoise ability for the reconstruction of multiple subsurface objects.**

***Index Terms*— Convolutional neural network (CNN), full-wave inversion (FWI), linear sampling method (LSM), subsurface reconstruction.**

I. Introduction

SUBSURFACE detection is important for both civilian and military activities. It has been widely used in archeology [1], buried pipe inspection [2], pavement crack surveys [3], landmine detection [4], environmental characterization [5], and so on.

Commonly used methods of subsurface detection include reverse time migration (RTM), Kirchhoff migration (KM), linear sampling method (LSM), and so on. The basic idea of RTM is to use the correlation between the incident wave and the reflected wave in the timestamp of the target space position [6]. By transmitting the reflected wave pulse recorded by the receiver back to the inversion domain, we can obtain the focused image of the target. RTM is the most accurate imaging method among the current migration methods without being affected by the tilt angle and the migration aperture [7]. However, its computational cost is unaffordable [8], especially for 3-D subsurface imaging. By contrast, KM is characterized by its simplicity [9] and still remains the most practical approach for 3-D prestack imaging. The principle of KM is to backpropagate the scalar wavefront observed at the receiver array to the imaging domain based on an integral solution of the scalar wave equation. The applicability of KM to electromagnetic (EM) imaging is because a vector wave equation can reduce to a scalar wave equation in a homogeneous isotropic medium. Unfortunately, the imaging effect of KM is not accurate as that of RTM. In addition, the cost of KM will also increase rapidly as the measurement scale increases [10]. As for LSM [11], its pivotal idea is to convert the EM field measured at the receiver array into the far-field spherically symmetric wave radiated by the fictitious focal source in the inversion domain. Compared with the previous two migration imaging methods, its calculation is faster. However, all these imaging methods are qualitative, that is to say, they can only reconstruct the positions and general shapes of the subsurface objects and cannot retrieve their dielectric constant values that are extremely essential for identifying these objects.

Full-wave inversion (FWI) is one of the most popular methods to quantitatively invert for both the geometry and dielectric parameters of the subsurface objects [12]. The traditional FWI method is to establish the objective function of the model parameters of the unknown objects first. It is usually the error functional of the modeled and the measured scattered fields [13]. Then, the optimal solutions of the model parameters are obtained by minimizing the objective function. However, there are two inherent drawbacks in EM FWI: ill-posedness and nonlinearity [14]. Ill-posedness is because the number of receivers is far less than the number of model parameters of unknown objects, which results in the instability and nonuniqueness of the FWI solution. Compared with that in the full-aperture EM inversion, the ill-posedness in the limited-aperture EM inversion is more severe. The most common method to mitigate the ill-posedness is adding the regularization term into the objective function to constrain the solution range [15]. Nonlinearity means the scattered EM field recorded at the receiver array changes nonlinearly with the unknown model parameters. As a result, iteration is inevitable in order to find them [16]. The frequently used iterative methods include Born iterative method (BIM) [17], contrast source inversion (CSI) [18], subspace optimization method (SOM) [19], and their variants [20], [21] as well as the hybridization [22], [23] and so on. However, the cost of these iterative algorithms is also high, especially for 3-D inversion problems.

Manuscript received July 4, 2021; revised August 2, 2021; accepted August 28, 2021. Date of publication September 8, 2021; date of current version January 21, 2022. This work was supported by the National Key Research and Development Program of the Ministry of Science and Technology of China under Grant 2018YFF01013300. *(Corresponding author: Feng Han.)*

The authors are with the Institute of Electromagnetics and Acoustics, Xiamen University, Xiamen 361005, China, and also with the Key Laboratory of Electromagnetic Wave Science and Detection Technology, Xiamen University, Xiamen 361005, China (e-mail: feng.han@xmu.edu.cn).

Digital Object Identifier 10.1109/TGRS.2021.3109086

1558-0644 © 2021 IEEE. Personal use is permitted, but republication/redistribution requires IEEE permission.
See https://www.ieee.org/publications/rights/index.html for more information.

In this study, we propose a threefold hybrid method to overcome the aforementioned shortcomings of EM FWI in the application of subsurface detection. Initially, we reconstruct the approximate shapes and positions of subsurface objects through the 3-D LSM [24]. However, the obtained shapes are relatively poor due to the limited aperture of the receiver array. Thus, we use a 3-D convolutional neural network (CNN) U-Net [25], [26] to perform certain repairs to obtain relatively more accurate shapes. Finally, we perform the FWI in the more accurate repaired regions using BIM. As the 3-D inversion domain is compressed, the number of unknowns used to depict the scatterers is reduced. The ill-posedness is alleviated. Simultaneously, the cost of iterative calculation is also greatly reduced. In addition, because the LSM calculation is fast and the neural network prediction is instantaneous, the additional computational cost of the hybrid method is negligible. It is worth mentioning that our hybrid method is different from the hybrid methods presented in [27] and [28]. In [27], the LSM is first used to estimate the supports of inhomogeneous scatterers, and then, the Born approximation is applied to the linearized scattering equation to obtain super-resolution scatterer images. In [28], the Gauss–Newton minimization assisted by the line search method is employed to reconstruct the dielectric objects from measured data with limited observation angles. However, our hybrid method is threefold. The LSM results are improved by the CNN. Then, the strictly rigorous iterative method BIM is used to invert for the dielectric parameters. It is also different from the learning-assisted inversion methods presented in [29] and [30], which first employs the neural network to obtain preliminary dielectric images of scatterers and then implements the FWI starting from these dielectric parameters. The CNN in our work is only used to classify the 3-D LSM images of scatterers buried in layered media in the way of voxel by voxel and thus downsize the inversion domain. The dielectric parameters of scatterers are completely obtained by BIM.

The organization of this article is given as follows. In Section II, the detailed description of the theory is presented, including the 3-D LSM in layered media, the 3-D FWI, and the 3-D U-Net. In Section III, two different application scenarios are used to verify the proposed hybrid method. In Section IV, the conclusion and future work are presented.

II. Methods

In this section, by combining with the conceptual diagram for a typical configuration of 3-D subsurface imaging and FWI, we first concisely introduce the principles and formulas of 3-D LSM in layered media. Then, the 3-D FWI in layered media is described briefly, including both the forward and inversion models. Finally, the 3-D CNN U-Net used to repair the LSM images is given in detail.

A. 3-D LSM in Layered Media

As shown in Fig. 1, the transmitter and receiver arrays denoted by Γ locate in the air. It is assumed that there are N_t transmitters and N_r receivers used in the measurement. The 3-D objects are buried in the homogeneous underground soil.

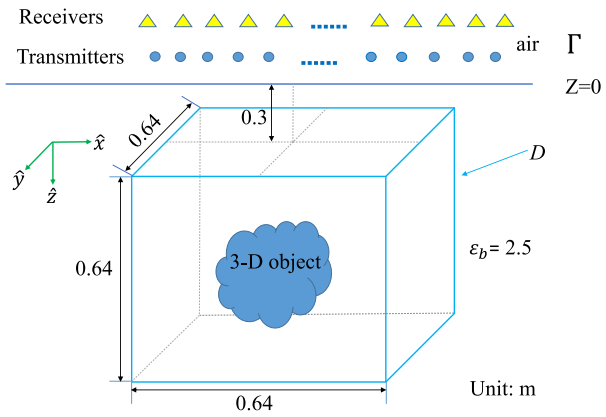

Fig. 1. Configuration of the 3-D imaging and FWI model.

The imaging and inversion domain denoted by D is discretized into a number of independent cells. The location of each cell is denoted by $\mathbf{r}_s$ which represents one spatial sampling point in the imaging domain. The 3-D LSM is to determine, for a certain frequency, the gain matching relationship between the scattered field data recorded at the receiver array and Green's function corresponding to the fictitious source point locating at $\mathbf{r}_s$. The obtained gain is expected to be a limited number if $\mathbf{r}_s$ lies inside the object but will be very large if it is outside the object [31].

The standard LSM formulation in 3-D vectorial geometry requires monochromatic multipolarization multiview multistatic data [24], [31]. Therefore, the incident field radiated by each transmitter provides two polarized components $(\hat{h}_i, \hat{h}_j)$, and for each polarization, it is necessary to measure the scattered field in two polarized directions $(\hat{p}_i, \hat{p}_j)$. Then, for each pair $(\hat{h}_i, \hat{p}_j)$, we have the $(N_t \times N_r)$-dimensional multistatic response data matrix $\mathbf{F}^{i,j}$ [31], whose generic element is the $\hat{p}_j$ polarized scattered field measured at the mth receiver when the nth transmitter emitts an $\hat{h}_i$ polarized EM field [24]. Assuming that the solution of 3-D LSM is the $(2N_r)$-dimensional unknown vector $\mathbf{g} = [\mathbf{g}_1(\mathbf{r}_s), \mathbf{g}_2(\mathbf{r}_s)]$, then the formula of LSM can be written as follows:

$$\mathbf{Fg} = \begin{bmatrix} \mathbf{F}^{1,1} & \mathbf{F}^{1,2} \\ \mathbf{F}^{2,1} & \mathbf{F}^{2,2} \end{bmatrix} \begin{bmatrix} \mathbf{g}_1(\mathbf{r}_s) \\ \mathbf{g}_2(\mathbf{r}_s) \end{bmatrix} = \begin{bmatrix} \mathbf{f}^1(\mathbf{r}_s) \\ \mathbf{f}^2(\mathbf{r}_s) \end{bmatrix} = \mathbf{f}(\mathbf{r}_s) \tag{1}$$

where $\mathbf{f}(\mathbf{r}_s)$ is composed of certain components of Green's functions and $\mathbf{g}$ is the indicator of the support of the scatterer.

In the layered media, we use the tangential components, i.e., the $\hat{x}$ or $\hat{y}$ polarized EM waves for 3-D LSM. Because a focused image still can be obtained even when the transmitted and received EM fields with the same polarization are used [24], we only retain two diagonal submatrices of $\mathbf{F}$ in (1). Besides, $\mathbf{f}(\mathbf{r}_s)$ contains the diagonal components of the layered medium dyadic Green's function (DGF) that connects the equivalent electric current in the imaging domain D and the electric field at the receiver array. In this way, (1) can be rewritten as follows:

$$\mathbf{Fg} = \begin{bmatrix} \mathbf{F}^{\hat{x}\hat{x}} & \mathbf{0} \\ \mathbf{0} & \mathbf{F}^{\hat{y}\hat{y}} \end{bmatrix} \begin{bmatrix} \mathbf{g}_1(\mathbf{r}_s) \\ \mathbf{g}_2(\mathbf{r}_s) \end{bmatrix} = \begin{bmatrix} \overline{\overline{\mathbf{G}}}_{\mathbf{EJ}}^{\hat{x}\hat{x}} \\ \overline{\overline{\mathbf{G}}}_{\mathbf{EJ}}^{\hat{y}\hat{y}} \end{bmatrix} \tag{2}$$

where $\overline{\overline{\mathbf{G}}}_{\mathbf{EJ}}$ is the layered medium DGF and its derivation can be found in [32]. Equation (2) is solved by transforming it into an optimization problem and adding the Tikhonov regularization term. Thus, we have

$$\hat{\mathbf{g}} = \arg\min_{\mathbf{g}} \|\mathbf{F}\mathbf{g} - \mathbf{f}\|_2^2 + \eta\|\mathbf{g}\|_2^2 \tag{3}$$

where η is the regularization factor and $\|\,\|_2$ denotes the L_2 norm. We choose this regularization because it guarantees smooth reconstructed LSM images. After a series of differential operation and matrix transformation, the final regularized solution can be simplified as

$$\hat{\mathbf{g}} = \left(\mathbf{F}^{\dagger}\mathbf{F} + \eta\mathbf{I}\right)^{-1}\mathbf{F}^{\dagger}\mathbf{f} \tag{4}$$

where $\dagger$ refers to the matrix hermitian and $\mathbf{I}$ denotes the identity matrix. Once $\hat{\mathbf{g}}$ is obtained, it is straightforward to judge whether $\mathbf{r}_s$ belongs to the object or the background by setting a threshold [31], and finally, we can acquire the 3-D shape of the object.

B. 3-D FWI in Layered Media

FWI is a data matching procedure, which utilizes the whole wavefield to obtain quantitative information of the unknown objects. It usually begins from an initial model and implements the forward computation. Then, simulated data and measured data are compared to adjust the model parameters of the unknown objects. This procedure repeats until the mismatches between simulated data and measured data are less than a threshold. In our work, the unknown subsurface objects are reconstructed. Thus, the FWI is implemented in the circumstance of layered media. As shown in Fig. 1, we assume that the transmitters and receivers are placed in the nth layer, while the unknown objects are buried in the mth layer. The electric field integral equation (EFIE) is adopted to formulate the forward and inverse scattering processes. We choose the integral equation because its computation domain D tightly wraps the subsurface objects and the unknowns in the discretized equation are limited. The forward scattering can be described by the state equation, which is expressed as

$$\mathbf{E}^m_{\text{inc}}(\mathbf{r}) = \mathbf{E}^m_{\text{tot}}(\mathbf{r}) - j\omega\varepsilon_b \int_D \overline{\overline{\mathbf{G}}}^{mm}_{\mathbf{EJ}}\left(\mathbf{r}, \mathbf{r}'\right) \cdot \chi\left(\mathbf{r}'\right)\mathbf{E}^m_{\text{tot}}\left(\mathbf{r}'\right) d\mathbf{r}' \tag{5}$$

where $\mathbf{E}^m_{\text{inc}}$ and $\mathbf{E}_{\text{tot}}$ are, respectively, referring to the incident electric field and the total electric field in the inversion domain D. In addition, χ is the contrast function of the object with respect to the background medium and defined as $\chi = (\epsilon/\epsilon_b - 1)$, where ϵ is the complex permittivity. The layered DGF $\overline{\overline{\mathbf{G}}}_{\mathbf{EJ}}$ is computed by the transmission line analogy [32]. In the forward scattering computation, (5) is discretized and the stabilized biconjugate gradient fast Fourier transform (BCGS-FFT) is employed to solve for $\mathbf{E}_{\text{tot}}$ in the inversion domain. Details can be found in [33] and [34] and will not be repeated here. Note that we choose the BCGS-FFT solver instead of using the direct solver because it can lower the computational time cost from $O(N^3)$ to $O(KN\log N)$, where K is the iteration number and N is the discrete unknowns in the computational domain [34].

The inverse scattering model is formulated by the data equation, which is expressed as

$$\mathbf{E}^n_{\text{sct}}(\mathbf{r}) = j\omega\varepsilon_b \int_D \overline{\overline{\mathbf{G}}}^{nm}_{\mathbf{EJ}}\left(\mathbf{r}, \mathbf{r}'\right) \cdot \chi\left(\mathbf{r}'\right)\mathbf{E}^m_{\text{tot}}\left(\mathbf{r}'\right) d\mathbf{r}' \tag{6}$$

where $\overline{\overline{\mathbf{G}}}^{nm}_{\mathbf{EJ}}$ is the DGF of the layered medium, which connects the equivalent electric current sources in the mth layer and the receivers in the nth layer. $\mathbf{E}^n_{\text{sct}}$ is the scattered field at the receiver array. FWI is to search for the optimized χ of (6) in all the discretized cells from $\mathbf{E}^n_{\text{sct}}$. We construct the L_2 norm cost function in the framework of BIM [17]

$$\mathbf{C}(\mathbf{x}_k) = \frac{\|\mathbf{b} - \mathbf{A}_k\mathbf{x}_k\|_2^2}{\|\mathbf{b}\|_2^2} + \gamma\,\frac{R(\mathbf{x}_k)}{R(\mathbf{x}_{k-1})} \tag{7}$$

in which $\mathbf{b}$ is a vector including the measured scattered field data, $\mathbf{A}$ is the Fréchet derivative matrix being composed of the DGF and the total field solved by BCGS-FFT, and $\mathbf{x}$ is a vector containing the unknown model parameters. The detailed elements of $\mathbf{b}$, $\mathbf{A}$, and $\mathbf{x}$ are listed in the Appendix. The subscript k means the kth iteration of BIM. Note that the matrix $\mathbf{A}$ also depends on the vector $\mathbf{x}$. Therefore, in BIM, $\mathbf{A}_k$ is assembled by DGF and the total field obtained by BCGS-FFT in the $(k-1)$th iteration. In this way, (7) is linearized. γ is the regularization factor and R is the total variational (TV) regularization, which is written as

$$R(\mathbf{x}) = \|\sqrt{(\mathbf{D}_x\mathbf{x})^2 + \left(\mathbf{D}_y\mathbf{x}\right)^2 + (\mathbf{D}_z\mathbf{x})^2}\|_1 \tag{8}$$

where $\|\cdot\|_1$ represents the L_1 norm and $\mathbf{D}_x$, $\mathbf{D}_y$, and $\mathbf{D}_z$ stand for the discrete difference matrices in three directions [35]. The purpose of TV regularization is to force the reconstructed scatterer to have a sharp boundary and smooth spatial distribution in the interior [36]. The square root in (8) acts on the sum of squares in the way of voxel by voxel. In each iteration step, the TV regularization is converted into the L_2 norm regularization by the reweighting method [35]. Consequently, the whole cost function (7) is in the form of L_2 norm. It can be minimized by solving its first derivative function using the conjugate gradient (CG) method [17], [37]. In the 3-D FWI, the initial model of BIM is the known background medium. Compared with LSM that only finds the scatterer support, FWI can directly invert for both the shape and dielectric parameters of the scatterer. However, because FWI needs to solve the nonlinear equation (7), iterations are inevitable. Therefore, (5) and (6) are solved alternately by the BCGS-FFT and BIM. This alternate iteration continues until the misfit between the measured scattered field and the calculated field reaches a stop criterion.

C. 3-D CNN U-Net

Because the image of the subsurface 3-D object reconstructed by LSM from the limited-aperture scattered field data recorded at the receiver array is poor, we use the traditional 3-D CNN U-Net given in [25] and [26] to repair it. The 3-D U-Net is originally proposed for segmenting biomedical images and classifies images at the voxel level. As shown in Fig. 2, the U-Net consists of a contracting path (the left side) and an expanding path (the right side), forming a U-shaped

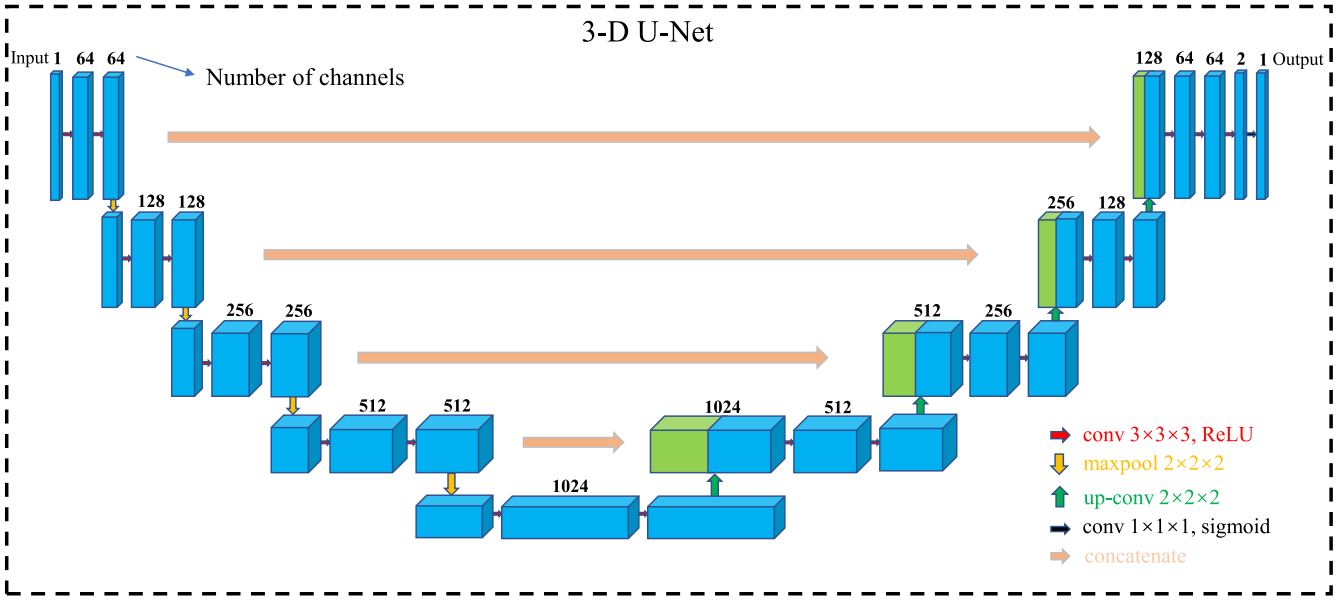

Fig. 2. Architecture of the 3-D CNN U-Net.

structure as a whole. The contraction path is used to obtain the context information, i.e., to extract the key features of the image in several steps of downsampling by convolutions with different kernels. By contrast, the expansion path is used for precise localization. Its function is to restore the main features of the entire image by upconvolutions. The contracting path follows the typical architecture of a convolutional network, which consists of four same parts. Each part includes two $3 \times 3 \times 3$ convolution layers with the ReLu activation function and $2 \times 2 \times 2$ max-pooling operation with stride 2 for downsampling. Through downsampling, the number of feature channels will be doubled. Symmetrically, the expansion path includes four parts as well, each of which has a $2 \times 2 \times 2$ upsampling convolution layer with the ReLu activation function and two $3 \times 3 \times 3$ convolution layers also with the ReLu activation function. It is worth noting that the concatenations between the layers in the contracting path and expansive path are used to compensate for the information loss in the downsampling. Besides, in the output layer, we set a 1×1 convolution layer with the sigmoid activation function.

As we all know, the loss function can well reflect the mismatch between the modeled and the actual sampling data. Here, we choose the Tversky loss [38] as the cost function for training, which can be expressed as

$$\text{Tversky Loss} = 1 - \frac{|\mathbf{P} \cap \mathbf{T}|}{|\mathbf{P} \cap \mathbf{T}| + \alpha|\mathbf{P} - \mathbf{T}| + \beta|\mathbf{T} - \mathbf{P}|} \tag{9}$$

where $\mathbf{T}$ is the true 3-D image of the object, i.e., the label used in the training, $\mathbf{P}$ is the predicted image, $|\mathbf{P} \cap \mathbf{T}|$ denotes the number of coincident voxels of $\mathbf{T}$ and $\mathbf{P}$, and $|\mathbf{P} - \mathbf{T}|$ refers to the number of voxels that are originally belonging to the background medium but are misjudged to belong to the object. Similarly, $|\mathbf{T} - \mathbf{P}|$ is the number of voxels that are originally belonging to the object but are misjudged to belong to the background medium. The hyperparameters α and β are the weights that control the magnitude of penalties for false positives and false negatives, respectively. When both α and β are equal to 0.5, the Tversky loss degenerates into the dice loss [39]. Note that there are two reasons for choosing the Tversky loss for our U-Net. One is that it is suitable for the situation where the number of positive samples ("object" voxels) is greatly different from that of negative samples ("background" voxels). In 3-D inversion problems, the positive samples are much less than negative samples. The other reason is that it directly uses evaluation indexes for training.

III. Numerical Results

In this section, we use two subsurface detection models: the ground penetrating radar (GPR) detection model and the subsurface drilling model to verify the feasibility of our proposed hybrid method. In the first GPR model, an inhomogeneous object with a complex shape is buried underground. The transmitter and receiver arrays are placed in the air. In the second subsurface drilling model, multiple homogeneous objects with different shapes are buried underground. Transmitters and receivers are placed inside the underground boreholes. In this case, the antinoise performance of the proposed hybrid method is also tested. In order to quantitatively evaluate the inversion performance, we introduce two indicators: the model misfit and the data misfit. The model misfit denotes the difference between the inverted dielectric parameters and the true parameters in all the discretized cells. The data misfit denotes the difference between the calculated and measured scattered fields at the receiver array. Their definitions are given in [40, eqs. (17) and (18)]. The operating frequency used for 3-D LSM is 2 GHz in both numerical cases but is lowered to 300 MHz in the FWI to ensure iteration stability. The regularization factor η in the LSM is empirically set as 0.004, while γ in the FWI is set as 0.005. With many times of experiments in this work, the weights α and β in the Tversky loss are set as 0.5. All the numerical experiments are performed on a workstation with 20-cores Xeon E2650 v3 2.3-G CPU, 512-GB RAM. The U-Net is trained on an NVIDIA Titan Xp

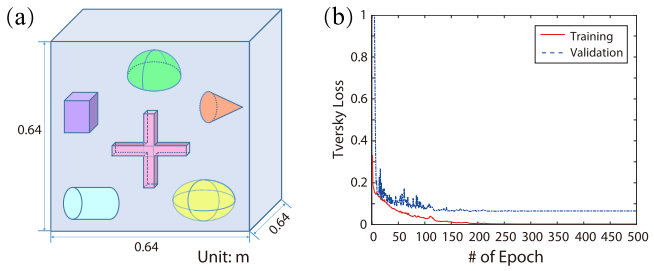

Fig. 3. (a) Basic geometry of the 3-D objects used for training U-Net in the GPR subsurface detection model. (b) Training and validation convergence curves.

GPU. In both numerical examples, the optimization method for U-Net is the Adam optimizer [41] with the hyperparameters $\beta_1 = 0.9$, $\beta_2 = 0.999$, $\epsilon = 0$, and the learning rate being equal to 5×10^{-4}.

A. Case 1: GPR Model

As shown in Fig. 1, the imaging and inversion domain has the dimensions of 0.64 m $\times$ 0.64 m $\times$ 0.64 m and is discretized into $32 \times 32 \times 32$ cells. The upper boundary of the inversion domain is at $z = 0.3$ m. The underground medium has a relative permittivity of 2.5. The unknown object buried inside it is inhomogeneous and has an irregular shape. The transmitter array locates at the $z_s = -0.2$ m plane and includes 8×8 transmitters. The distance between two transmitters is 0.3 m. The receiver array locates at the $z_r = -0.4$ m plane and consists of 8×8 receivers with the interval of 0.3 m between two. All transmitters and receivers are used when the 3-D LSM is implemented. However, only 6×6 transmitters and 6×6 receivers are used for FWI. For the U-Net, the input is the 3-D LSM image having gray values. Its output is the 3-D binary image. The dimensions of both the input and the output are $32 \times 32 \times 32$.

As shown in Fig. 3(a), the training dataset of U-Net contains a total of six 3-D simple shapes, including ellipsoids, cylinders, cones, hemispheres, cuboids, and the random combinations of cuboids. We combine the cuboids to form the concave shapes, e.g., a cross, and let the U-Net learn it in the training. Each sample in the training dataset has one of the above shapes, and it randomly exists in any position of the inversion domain with different sizes. The relative permittivity of the object randomly changes between 2.8 and 4.0. Totally, we randomly generate 1100 3-D samples. Among them, 1000 samples are used for training and 100 ones are for validation. The inputs of U-Net are the 3-D shapes reconstructed by LSM. Its labels are the true shapes. As shown in Fig. 3(b), after 500 epochs of training, the training loss stably remains 0.003, while the validation loss stably remains 0.07. These low loss values not only guarantee the reconstructed shape resembling the true shape but also ensure the compressed inversion domain containing the whole unknown objects in a large probability.

Although the 3-D U-Net is trained only by homogeneous objects, inhomogeneous objects formed by combing different homogeneous simple shapes are used in the testing. As shown in the first and second columns of Fig. 4, an "L" shape, a mushroom, a warehouse, and an ice cream are used to test the LSM algorithm and the U-Net. The LSM images shown in the third and fourth columns are obtained by

$$G(\mathbf{r}_s) = -\log(\hat{\mathbf{g}}(\mathbf{r}_s) \cdot \hat{\mathbf{g}}(\mathbf{r}_s)). \tag{10}$$

A direct observation is that the 2-D slices in the xy plane are much closer to the true shapes than those in the xz plane. The reason is that both the transmitter and receiver arrays locate in the xy plane. The array aperture is large enough in the horizontal direction but very limited in the vertical direction. By utilizing a threshold to limit the voxel classification, we obtain the 3-D LSM results of the subsurface objects via brutal cut and they are shown in the fifth column of Fig. 4. The threshold is selected by multiplying the maximum value of the LSM values in all the voxels in the imaging domain by an empirical constant, which can be expressed as

$$\text{threshold} = C \max_{\mathbf{r}_s} G(\mathbf{r}_s) \tag{11}$$

where the empirical constant C is adjustable for the best shape to contain the whole scatterers [31]. The sixth column in Fig. 4 shows the 3-D LSM images repaired by the U-Net. Obviously, compared with the results shown in the fifth column, the 3-D images by U-Net get great improvements by significant repairments of the distorted shapes in the xz plane and the 3-D shapes become very close to true shapes.

Then, we conduct comparative experiments of FWI by BIM to reconstruct the permittivity of the four subsurface objects in Tests #1–4, as shown in the first and second columns of Fig. 4. The inversion is implemented in the whole inversion domain, the imaging region judged via the threshold classification, and the imaging region judged via the U-Net classification. The results are shown in Fig. 5. Three observations are made. First, due to the single-sided illumination and limited aperture of the antenna array, the inversion results by BIM implemented in the whole inversion domain are far from the ground truths, which is reflected in the much larger reconstructed shapes and excessively smaller inverted permittivities compared to the ground truths. Second, performing FWI in the imaging region judged via the threshold classification also fails to obtain good results although the computational cost significantly lowered since the 3-D inversion domain is reduced. The inversion results are shown in the second and fifth columns of Fig. 5. We can see that the reconstructed shapes resemble the true shapes only in the xy plane but are distorted obviously in the xz plane. This is also illustrated by the LSM images shown in the third and fourth columns of Fig. 4. In addition, the inverted permittivity values are also different from the true parameters. This once again shows that the standard LSM imaging method for the reconstruction of 3-D objects from limited-aperture EM data has great limitations. Third, the aforementioned drawbacks can be compensated by the 3-D U-Net, which effectively restores the subsurface object shapes, and thus, the FWI is implemented in a more accurate inversion domain. The reconstructed results are shown in the third and sixth columns of Fig. 5. We can see that both the shapes and permittivity values are close to the ground truths.

Fig. 6 shows the variations of data misfits in Tests #1–4 for all three types of inversion. Due to single-sided illumination

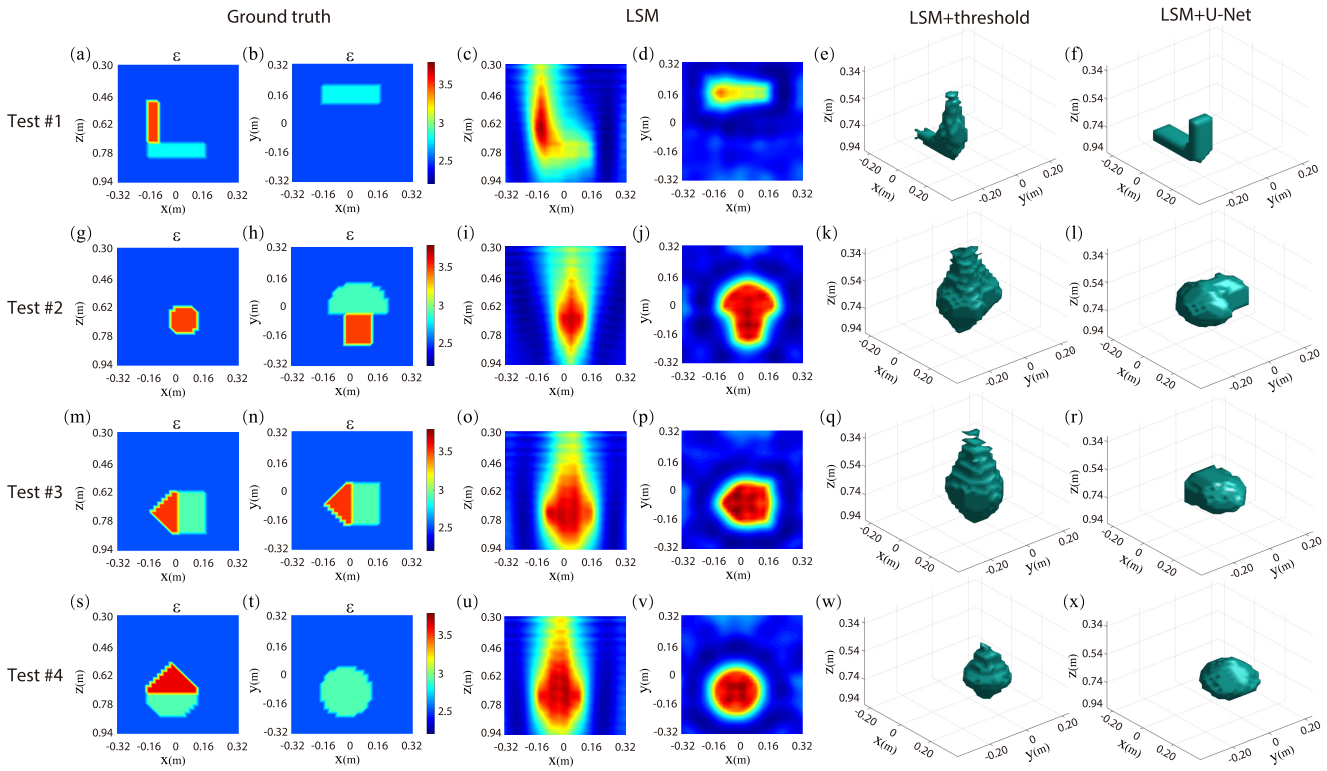

Fig. 4. Ground truths, LSM imaging results, and the voxel classification results in the four tests. Columns 1 and 3 show the 2-D xz slices. Columns 2 and 4 show the 2-D xy slices. Column 5 shows the LSM results based on the threshold cut. Column 6 shows the LSM results based on 3-D U-Net.

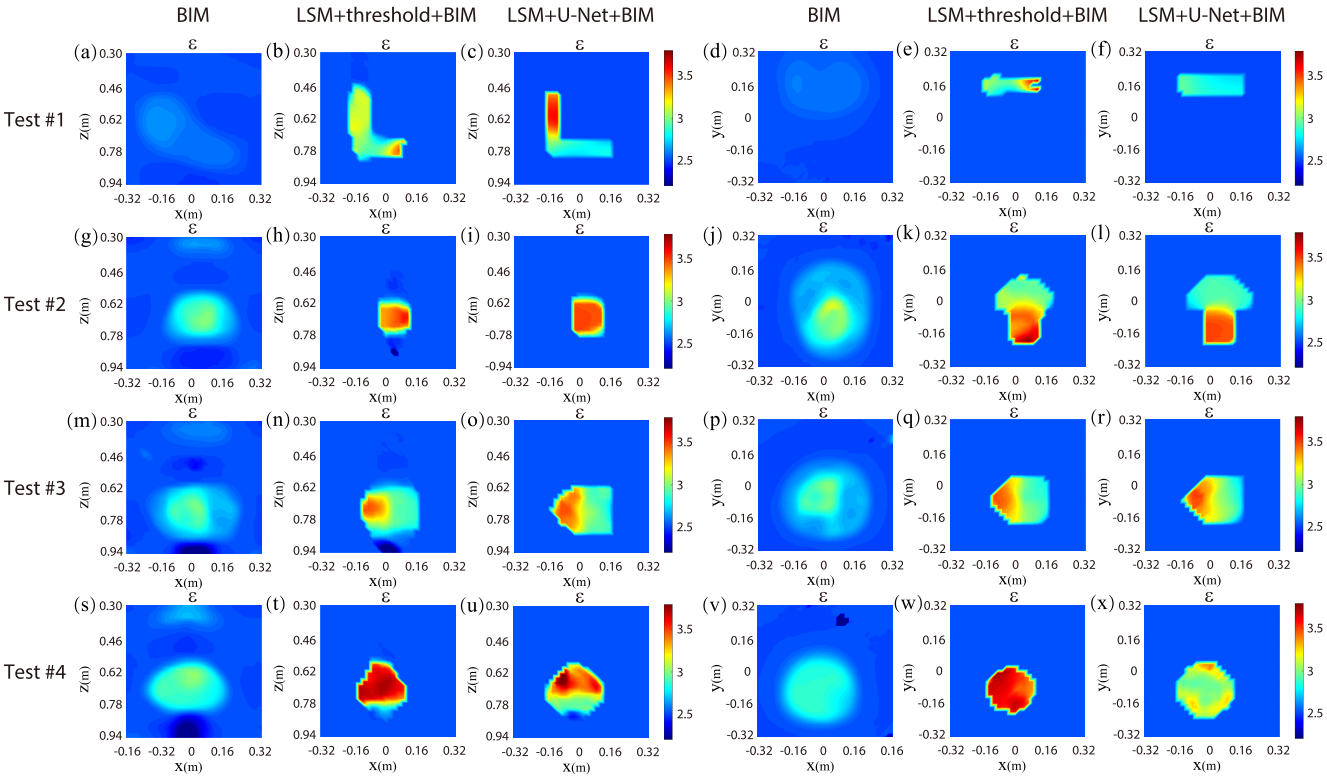

Fig. 5. FWI results by BIM implemented in the whole inversion domain, the imaging region judged via the threshold classification, and the imaging region judged via the U-Net classification. Columns 1–3 show the 2-D xz slices of inversion results. Columns 4–6 show the 2-D xy slices of inversion results.

and limited aperture, among the three types of inversion, FWI implemented in the whole region has the largest data misfit. By contrast, because the restored shapes by U-Net coincide with the true shapes well, the FWI implemented in the imaging region judged via the U-Net classification has the smallest data misfit. Another obvious comparison is the computational

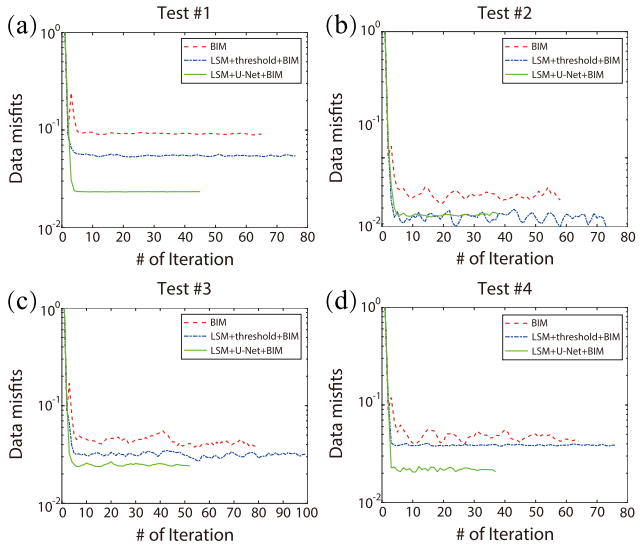

Fig. 6. Comparisons of convergence curves of BIM for the three methods in the four tests.

TABLE I

MODEL MISFITS (%) FOR BIM, LSM+TH+BIM, AND LSM+U-NET+BIM

Test \ Method		BIM	LSM+TH+BIM	LSM+U-Net+BIM
Test #1	ε	2.824	0.653	0.652
Test #2	ε	2.123	2.482	2.091
Test #3	ε	3.412	2.235	1.673
Test #4	ε	4.604	3.862	2.548

Remark: TH represents "threshold".

cost. For example, in Test #1, totally, there are 32 768, 554, and 459 discretized cells for the whole inversion domain, the inversion domain judged via the threshold classification, and the inversion domain judged via the U-Net classification, respectively, that is to say, the computational cost of the proposed threefold hybrid method is also the lowest. Table I lists the model misfits of reconstructed permittivity values when the iterations terminate. It can be seen that among the three methods, the FWI implemented in the region judged via the U-Net classification has the smallest model misfit.

B. Case 2: Subsurface Drilling Model

The subsurface drilling model is shown in Fig. 7. The inversion domain enclosing the objects has the dimensions of 0.64 m × 0.64 m × 1.28 m and is discretized into 32 × 32 × 64 cells. Therefore, the input and output of the U-Net, in this case, have the dimensions of 32 × 32 × 64. The underground medium has the relative permittivity of 2.5 and conductivity of 1 mS/m. Eight receivers and eight transmitters are placed in each borehole. Eight boreholes are drilled around the inversion domain, and the locations are shown on the right of Fig. 7. All these transmitters and receivers are used in the 3-D LSM imaging. However, only six transmitters in each borehole and six receivers in each borehole are used in the FWI. As shown in Fig. 8(a), the basic shapes of the 3-D objects used in the training dataset are the same as those in Case 1. However, multiple homogeneous objects with different shapes are allowed to be placed inside the inversion domain.

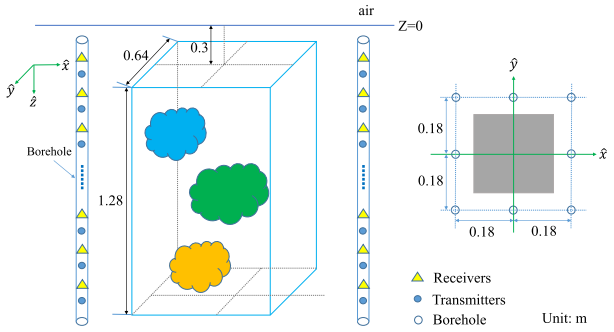

Fig. 7. Configuration of the 3-D subsurface drilling model.

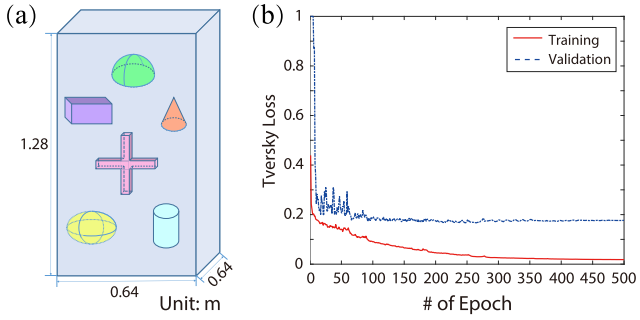

Fig. 8. (a) Basic geometry of the 3-D objects used for training U-Net in the subsurface drilling model. (b) Training and validation convergence curves.

Therefore, for each training sample, two or three objects coexist without overlapping each other. The relative permittivity values of the objects distribute randomly between 2.8 and 4.0. Meanwhile, their conductivities are assigned random values between 1 and 5 mS/m. In order to enhance the antinoise ability of the proposed hybrid method, we contaminate the simulated scattered field with 20-dB white Gaussian noise, which leads to approximately 10% errors of the data. Here, the noise level is defined according to the signal-to-noise ratio (SNR) of power. Similar to Case 1, we also set up 1000 training samples and 100 validation samples and train the U-Net for 500 000 epochs. The loss variation curves are shown in Fig. 8(b). We can see that the training loss and validation loss finally stably remain as 0.02 and 0.18, respectively, which are much larger than those shown in Fig. 3(b). One important reason for this phenomenon is the existence of multiple objects inside the inversion domain, which leads to mutual scattering. Consequently, the LSM images become worse and the learning task becomes more difficult for U-Net.

In the online prediction, we choose three models that include one, two, and three homogeneous objects. The ground truths of these testing models are shown in Fig. 9. Test #5 has only one "H"-shaped object whose relative permittivity value exceeds the maximum permittivity 4.0 in the training dataset. The inversion domain in Test #6 includes a sphere and a cube. Test #7 is challenging since it has three objects buried underground. They are a cone, a cube, and a warehouse. In addition, we also verify the antinoise ability of our method by comparing the reconstruction results for the simulated scattered field data contaminated by noise with different levels. The imaging results are shown in Fig. 10. The first three columns show the LSM results of the three models under

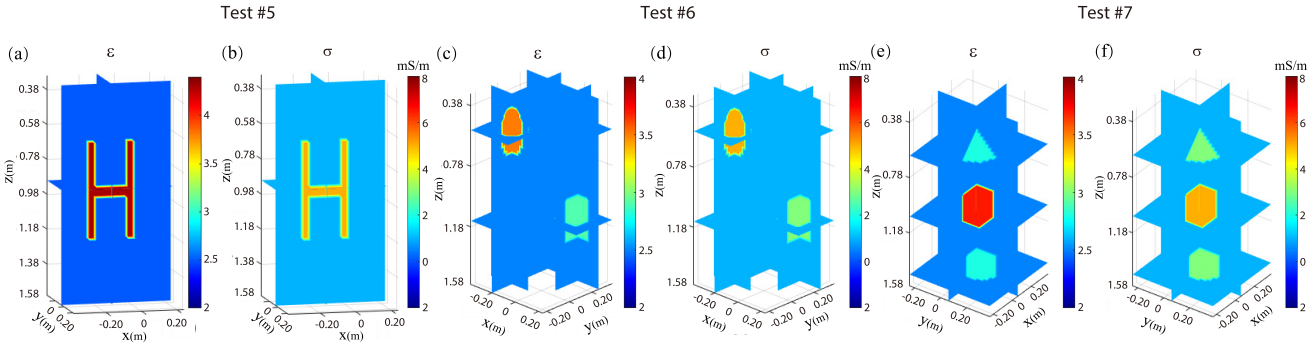

Fig. 9. Ground truths of three tests in Case 2.

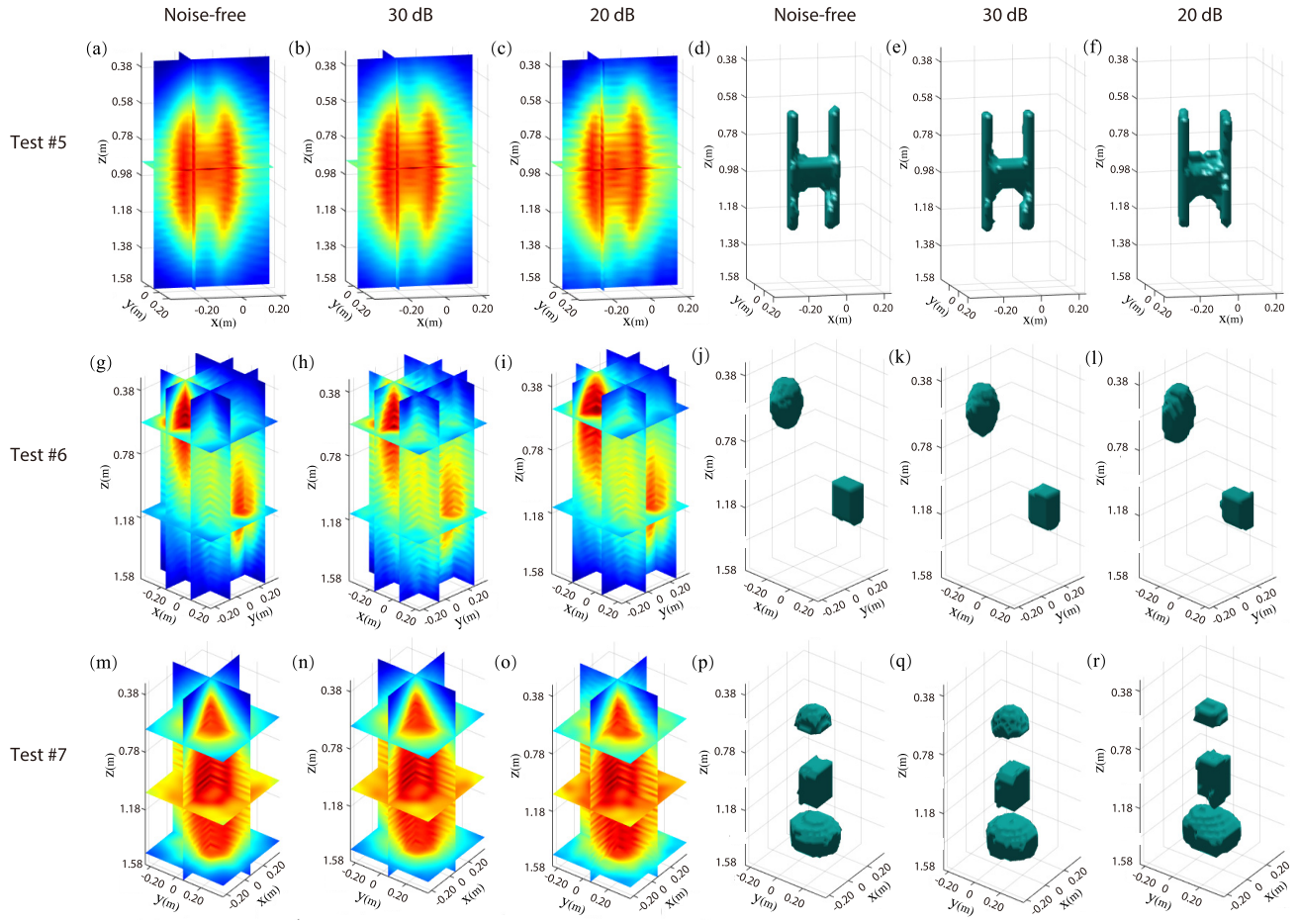

Fig. 10. LSM results and U-Net classification results under three different noise levels. Columns 1–3 show the LSM results. Columns 4–6 show the U-Net classification results.

different noise levels. The last three columns are the 3-D images by U-net recovery.

Obviously, as the noise increases, both the LSM images and the shapes recovered by U-Net become worse and worse. Another interesting observation is the comparison among the results for the three models. We can see that the "H" shape in the imaging results is still discernible even when the scattered field data are contaminated by 20-dB noise. This is clearly shown in Fig. 10(c). However, when there are two objects coexisting in the inversion domain, the limitation of the standard LSM is clearly manifested. We can only see that there are two objects in the LSM images, as shown in Fig. 10(g)–(i). Their shapes are severely distorted. When there are three objects, the LSM images of three objects stick together. It seems that there is only one object in the imaging domain, as shown in Fig. 10(m)–(o). Fortunately, both the distorted shapes and indiscernible objects can be effectively recovered by the trained 3-D U-Net. The results are shown in columns 4–6 of Fig. 10. We can see that the restored shapes in Tests #5 and 6 are roughly consistent with the ground truths even when the 20-dB noise is added. In Test #7, the tip of the cone is lost in the U-Net results. The cone is restored to be a half-sphere when noise free. It even becomes a cube when 20-dB noise is added. In other words, although the U-net

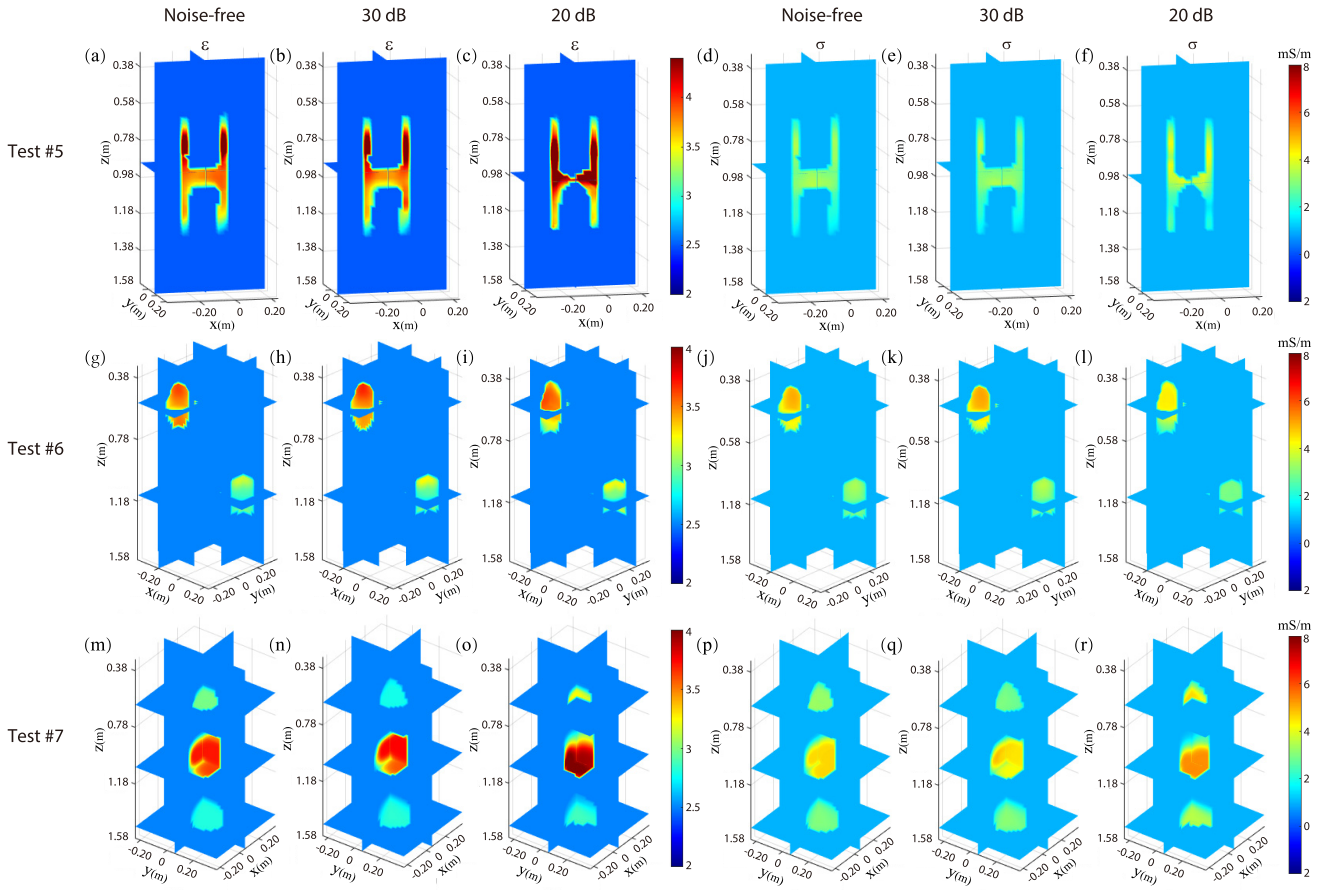

Fig. 11. FWI results by BIM implemented in the imaging region judged via the U-Net classification under three different noise levels. Columns 1–3 show the reconstructed permittivity. Columns 4–6 show the reconstructed conductivity.

TABLE II

MODEL MISFITS (%) OF INVERTED PARAMETERS WHEN THE SCATTERED FIELD DATA ARE CONTAMINATED BY NOISE WITH DIFFERENT SNRS

Test \ noise-level		noise-free	30 dB	20 dB
Test #5	ε	2.993	2.975	3.794
	σ	17.878	18.176	20.987
Test #6	ε	1.789	1.691	1.905
	σ	16.008	16.712	17.962
Test #7	ε	2.104	1.920	2.875
	σ	19.632	20.384	25.914

can improve LSM imaging results, shape distortion cannot be absolutely avoided, especially when the measured scattered field data are contaminated by large noise or when the shape of the object is too irregular.

Finally, we perform FWI by BIM based on the results of U-Net recovery to obtain the dielectric parameters of the subsurface objects. The results are shown in Fig. 11. By comparing with the ground truths shown in Fig. 9, the FWI implemented in the imaging region judged via the U-Net classification can effectively reconstruct both the permittivity and the conductivity of multiple subsurface objects even when they have irregular shapes. Of course, due to the addition of noise and the limitation of LSM itself, the deviation of the inverted model parameters from the true values is also inevitable. This is clearly shown in Fig. 11(o) and (r). Table II lists the model misfits of Tests #5–7 under three different noise levels. Obviously, as the noise level increases, the model misfits increase. This is because the LSM images become worse when the scattered field data are contaminated by noise. The recovered images by U-Net then also become worse, and thus, the compressed inversion domain deviates away from the true shape of the object. Another observation is that the model misfits become larger and larger from Tests #5 and #7. For multiple objects buried in the underground inversion domain, mutual EM scattering takes the effect. The nonlinearity will deteriorate both the LSM imaging and FWI results.

IV. CONCLUSION AND FUTURE WORK

In this article, we propose a threefold hybrid EM FWI method to reconstruct the subsurface objects when the antenna array has the limited aperture. The method includes three steps. First, the 3-D LSM is employed to qualitatively reconstruct the shapes and locations of the underground objects. Compared with the iterative FWI methods, e.g., BIM, the computational time of LSM is negligible. However, the images obtained by LSM have poor quality due to the limited illumination angle. Therefore, in the second step, we improve the images by using a 3-D U-Net. Finally, in the FWI phase, we implement BIM in the imaging region judged via the U-Net classification to reconstruct the dielectric parameters of subsurface inhomogeneous objects or multiple homogeneous objects in different scenarios.

In order to validate the feasibility and efficiency of the proposed subsurface detection method, we apply it to two different scenarios: the GPR detection and the subsurface drilling detection. We conducted a series of comparative experiments, including the performance comparison with the traditional inversion method and comparisons of inversion results under different noise levels. Experimental results show that this method has excellent performance on inversion, which effectively reduces the ill-posedness, improves the inversion accuracy, reduces the amount of calculation, as well as has a certain antinoise performance. At the same time, the inversion experiments in these two scenarios also show the possible applications of our method in practical engineering measurements.

In recent years, with the continuous increase of infrastructure and the increasing emphasis on shallow ground resources, the development of underground space has gradually accelerated, and the research on subsurface detection technology has also increased. The future work of our research will be focused on many practical subsurface detection applications such as unexploded object detection. The proposed hybrid method will be used to invert the field measured data to obtain high-accuracy parameters of unknown objects buried underground.

APPENDIX

Equation (6) can be discretized and written as

$$\mathbf{b}' = \mathbf{A}'\mathbf{x}' \tag{A1}$$

where

$$\mathbf{b}' = \left[\mathbf{E}^n_{\text{sct}}(\mathbf{r}_{iR}, \mathbf{r}_{iT})\right] \in \mathbb{C}^{(2N_tN_r,1)} \tag{A2a}$$

$$\mathbf{A}' = j\omega\Delta V\left[\overline{\overline{\mathbf{G}}}^{nm}_{\mathbf{EJ}}\left(\mathbf{r}_{iR}, \mathbf{r}'_k\right)\mathbf{E}^m_{\text{tot}}\left(\mathbf{r}'_k, \mathbf{r}_{iT}\right)\right] \in \mathbb{C}^{\left(2N_tN_r, N_xN_yN_z\right)} \tag{A2b}$$

$$\mathbf{x}' = \left[\left(\varepsilon\left(\mathbf{r}'_k\right) - \varepsilon_b\right) + \left(\frac{\sigma\left(\mathbf{r}'_k\right) - \sigma_b}{j\omega}\right)\right] \in \mathbb{C}^{\left(1, N_xN_yN_z\right)}. \tag{A2c}$$

Note that only two horizontal electric components are used in the inversion. $iT \in [1, N_t]$, $iR \in [1, N_r]$, and $k \in [1, N_xN_yN_z]$ are the indexes of transmitters, receivers, and discrete voxels in the inversion domain, respectively. ΔV is the volume of a discrete voxel. Equation (A1) is a complex-number equation and a real-number equation can be obtained by splitting it

$$\mathbf{b} = \mathbf{A}\mathbf{x} \tag{A3}$$

where

$$\mathbf{b} = \begin{bmatrix}\text{Re}\left(\mathbf{b}'\right) \\ \text{Im}\left(\mathbf{b}'\right)\end{bmatrix} \in \mathbb{R}^{(4N_tN_r,1)} \tag{A4a}$$

$$\mathbf{A} = \begin{bmatrix}\text{Re}\left(\mathbf{A}'\right) & \dfrac{\text{Im}\left(\mathbf{A}'\right)}{j\omega} \\ \text{Im}\left(\mathbf{A}'\right) & -\dfrac{\text{Re}\left(\mathbf{A}'\right)}{j\omega}\end{bmatrix} \in \mathbb{R}^{\left(4N_tN_r, 2N_xN_yN_z\right)} \tag{A4b}$$

$$\mathbf{x} = \begin{bmatrix}\left(\varepsilon\left(\mathbf{r}'_k\right) - \varepsilon_b\right) \\ \sigma\left(\mathbf{r}'_k\right) - \sigma_b\end{bmatrix} \in \mathbb{R}^{\left(1, 2N_xN_yN_z\right)}. \tag{A4c}$$

REFERENCES

[1] W. Zhao *et al.*, "Advances in GPR data acquisition and analysis for archaeology," *Geophys. J. Int.*, vol. 202, no. 1, pp. 62–71, 2015.

[2] H. Liu, X. Huang, F. Han, J. Cui, B. F. Spencer, and X. Xie, "Hybrid polarimetric GPR calibration and elongated object orientation estimation," *IEEE J. Sel. Topics Appl. Earth Observ. Remote Sens.*, vol. 12, no. 7, pp. 2080–2087, Jul. 2019.

[3] H. Li, D. Song, Y. Liu, and B. Li, "Automatic pavement crack detection by multi-scale image fusion," *IEEE Trans. Intell. Transp. Syst.*, vol. 20, no. 6, pp. 2025–2036, Jun. 2019.

[4] X. Feng and M. Sato, "Pre-stack migration applied to GPR for landmine detection," *Inverse Problems*, vol. 20, no. 6, pp. S99–S115, Dec. 2004.

[5] G. A. Newman and G. M. Hoversten, "Solution strategies for two- and three-dimensional electromagnetic inverse problems," *Inverse Problems*, vol. 16, no. 5, pp. 1357–1375, Oct. 2000.

[6] H. Liu, Z. Long, F. Han, G. Fang, and Q. H. Liu, "Frequency-domain reverse-time migration of ground penetrating radar based on layered medium Green's functions," *IEEE J. Sel. Topics Appl. Earth Observ. Remote Sens.*, vol. 11, no. 8, pp. 2957–2965, Aug. 2018.

[7] J. Zhu and L. R. Lines, "Comparison of Kirchhoff and reverse-time migration methods with applications to prestack depth imaging of complex structures," *Geophysics*, vol. 63, no. 4, pp. 1166–1176, Jul. 1998.

[8] F. Deng and G. A. Mcmechan, "True-amplitude prestack depth migration," *Geophysics*, vol. 72, no. 3, pp. S155–S166, May 2007.

[9] X. Zhuge, A. G. Yarovoy, T. Savelyev, and L. Ligthart, "Modified Kirchhoff migration for UWB MIMO array-based radar imaging," *IEEE Trans. Geosci. Remote Sens.*, vol. 48, no. 6, pp. 2692–2703, Jun. 2010.

[10] R. Rastogi, A. Srivastava, K. Khonde, K. M. Sirasala, A. Londhe, and H. Chavhan, "An efficient parallel algorithm: Poststack and prestack Kirchhoff 3D depth migration using flexi-depth iterations," *Comput. Geosci.*, vol. 80, pp. 1–8, Jul. 2015.

[11] I. Catapano, L. Crocco, and T. Isernia, "On simple methods for shape reconstruction of unknown scatterers," *IEEE Trans. Antennas Propag.*, vol. 55, no. 5, pp. 1431–1436, May 2007.

[12] S. Lambot, E. C. Slob, I. V. D. Bosch, B. Stockbroeckx, and M. Vanclooster, "Modeling of ground-penetrating radar for accurate characterization of subsurface electric properties," *IEEE Trans. Geosci. Remote Sens.*, vol. 42, no. 11, pp. 2555–2568, Nov. 2004.

[13] C. Yu, M. Yuan, and Q. H. Liu, "Reconstruction of 3D objects from multi-frequency experimental data with a fast DBIM-BCGS method," *Inverse Probl.*, vol. 25, no. 2, pp. 1–24, Feb. 2009.

[14] X. Chen, Ed., *Computational Methods for Electromagnetic Inverse Scattering*. Singapore: Wiley, 2018.

[15] Y. Chen, J. Li, L. Wang, F. Han, and Q. H. Liu, "Multiparametric electromagnetic inversion of 3-D anisotropic objects embedded in layered media based on mixed $L_1 - L_2$ norm regularization," *IEEE Antennas Wireless Propag. Lett.*, vol. 20, no. 5, pp. 738–742, May 2021.

[16] Y. M. Wang and W. C. Chew, "An iterative solution of the two-dimensional electromagnetic inverse scattering problem," *Int. J. Imag. Syst. Technol.*, vol. 1, no. 1, pp. 100–108, Jun. 1989.

[17] F. Li, Q. H. Liu, and L.-P. Song, "Three-dimensional reconstruction of objects buried in layered media using Born and distorted Born iterative methods," *IEEE Geosci. Remote Sens. Lett.*, vol. 1, no. 2, pp. 107–111, Apr. 2004.

[18] P. M. van den Berg and R. E. Kleinman, "A contrast source inversion method," *Inverse Problems*, vol. 13, no. 6, pp. 1607–1620, 1997.

[19] X. Chen, "Subspace-based optimization method for solving inverse-scattering problems," *IEEE Trans. Geosci. Remote Sens.*, vol. 48, no. 1, pp. 42–49, Aug. 2010.

[20] D. W. Winters, J. D. Shea, P. Kosmas, B. D. Van Veen, and S. C. Hagness, "Three-dimensional microwave breast imaging: Dispersive dielectric properties estimation using patient-specific basis functions," *IEEE Trans. Med. Imag.*, vol. 28, no. 7, pp. 969–981, Jul. 2009.

[21] N. Zaiping, Y. Feng, Z. Yanwen, and Z. Yerong, "Variational Born iteration method and its applications to hybrid inversion," *IEEE Trans. Geosci. Remote Sens.*, vol. 38, no. 4, pp. 1709–1715, Jul. 2000.

[22] K. Xu, Y. Zhong, R. Song, X. Chen, and L. Ran, "Multiplicative-regularized FFT twofold subspace-based optimization method for inverse scattering problems," *IEEE Trans. Geosci. Remote Sens.*, vol. 53, no. 2, pp. 841–850, Feb. 2015.

[23] X. Ye and X. Chen, "Subspace-based distorted-Born iterative method for solving inverse scattering problems," *IEEE Trans. Antennas Propag.*, vol. 65, no. 12, pp. 7224–7232, Dec. 2017.

[24] I. Catapano, L. Crocco, and T. Isernia, "Improved sampling methods for shape reconstruction of 3-D buried targets," *IEEE Trans. Geosci. Remote Sens.*, vol. 46, no. 10, pp. 3265–3273, Oct. 2008.

[25] O. Çiçek, A. Abdulkadir, S. Lienkamp, T. Brox, and O. Ronneberger, "3D U-Net: Learning dense volumetric segmentation from sparse annotation," in *Proc. Int. Conf. Med. Image Comput. Comput.-Assist. Intervent. (MICCAI)*. Cham, Switzerland: Springer, 2016, pp. 424–432.
[26] J. Xiao, J. Li, Y. Chen, F. Han, and Q. H. Liu, "Fast electromagnetic inversion of inhomogeneous scatterers embedded in layered media by Born approximation and 3-D U-Net," *IEEE Geosci. Remote Sens. Lett.*, vol. 17, no. 10, pp. 1677–1681, Oct. 2020.
[27] M. Brignone, J. Coyle, and M. Piana, "The use of the linear sampling method for obtaining super-resolution effects in Born approximation," *J. Comput. Appl. Math.*, vol. 203, no. 1, pp. 145–158, 2007.
[28] J. Zhang, K. Yang, and M. S. Tong, "Inversion of scattering data for reconstructing dielectric objects with limited observation angles," *IEEE Antennas Wireless Propag. Lett.*, vol. 13, pp. 83–86, 2014.
[29] G. Chen, P. Shah, J. Stang, and M. Moghaddam, "Learning-assisted multimodality dielectric imaging," *IEEE Trans. Antennas Propag.*, vol. 68, no. 3, pp. 2356–2369, Mar. 2020.
[30] P. Mojabi, V. Khoshdel, and J. Lovetri, "Tissue-type classification with uncertainty quantification of microwave and ultrasound breast imaging: A deep learning approach," *IEEE Access*, vol. 8, pp. 182092–182104, 2020.
[31] D. Colton, H. Haddar, and M. Piana, "The linear sampling method in inverse electromagnetic scattering theory," *Inverse Problems*, vol. 19, no. 6, pp. S105–S137, Nov. 2003.
[32] K. A. Michalski and J. R. Mosig, "Multilayered media Green's functions in integral equation formulations," *IEEE Trans. Antennas Propag.*, vol. 45, no. 3, pp. 508–519, Mar. 1997.
[33] X. Millard and Q. H. Liu, "A fast volume integral equation solver for electromagnetic scattering from large inhomogeneous objects in planarly layered media," *IEEE Trans. Antennas Propag.*, vol. 51, no. 9, pp. 2393–2401, Sep. 2003.
[34] X. Millard and Q. H. Liu, "Simulation of near-surface detection of objects in layered media by the BCGS-FFT method," *IEEE Trans. Geosci. Remote Sens.*, vol. 42, no. 2, pp. 327–334, Feb. 2004.
[35] B. Wohlberg and P. Rodriguez, "An iteratively reweighted norm algorithm for minimization of total variation functionals," *IEEE Signal Process. Lett.*, vol. 14, no. 12, pp. 948–951, Dec. 2007.
[36] P. Rodríguez, "Total variation regularization algorithms for images corrupted with different noise models: A review," *J. Electr. Comput. Eng.*, vol. 2013, pp. 1–18, 2013.
[37] M. F. Catedra, R. P. Torres, J. Basterrechea, and E. Gago, Eds., *CG-FFT Method: Application of Signal Processing Techniques to Electromagnetics*. Boston, MA, USA: Artech House, 1994.
[38] S. S. M. Salehi, D. Erdogmus, and A. Gholipour, "Tversky loss function for image segmentation using 3D fully convolutional deep networks," in *Proc. Int. Workshop Mach. Learn. Med. Imag.*, Montreal, QC, Canada: Springer, 2017, pp. 379–387.
[39] F. Milletari, N. Navab, and S.-A. Ahmadi, "V-Net: Fully convolutional neural networks for volumetric medical image segmentation," in *Proc. 4th Int. Conf. 3D Vis. (3DV)*, Oct. 2016, pp. 565–571.
[40] T. Lan, N. Liu, F. Han, and Q. H. Liu, "Joint petrophysical and structural inversion of electromagnetic and seismic data based on volume integral equation method," *IEEE Trans. Geosci. Remote Sens.*, vol. 57, no. 4, pp. 2075–2086, Apr. 2019.
[41] D. P. Kingma and J. Ba, "Adam: A method for stochastic optimization," 2014, *arXiv:1412.6980*. [Online]. Available: http://arxiv.org/abs/1412.6980

Miao Zhong received the B.S. degree in communication engineering from Nanchang Hangkong University of China, Nanchang, China, in 2020. She is currently pursuing the master's degree with Xiamen University, Xiamen, China.

Her research interests include electromagnetic inverse scattering and full-wave inversion.

Yanjin Chen received the B.S. degree in mechanical and electronic engineering from Hainan University of China, Haikou, Hainan, China, in 2017, and the M.S. degree in the electromagnetic field and wireless technology from Xiamen University, Xiamen, China, in 2021.

He is currently a Research Assistant at Fujian Provincial Key Laboratory of Electromagnetic Wave Science and Detection Technology, Xiamen University. His research interest is applying machine learning techniques to electromagnetic inverse scattering problems.

Jiawen Li received the B.S. degree in electronic science and technology from Wuhan University of Technology of China, Wuhan, China, in 2011. He is currently pursuing the Ph.D. degree with Xiamen University, Xiamen, China.

His research interests include electromagnetic scattering and inverse scattering in complex media and the full-wave inversion of anisotropic targets.

Feng Han (Senior Member, IEEE) received the B.S. degree in electronic science from Beijing Normal University, Beijing, China, in 2003, the M.S. degree in geophysics from Peking University, Beijing, in 2006, and the Ph.D. degree in electrical engineering from Duke University, Durham, NC, USA, in 2011.

Since July 2015, he has been with Xiamen University, where he is currently an Associate Professor with the Institute of Electromagnetics and Acoustics. He has published over 40 articles in refereed journals. His research interests include electromagnetic scattering and inverse scattering in complex media, fast full-wave electromagnetic inversion based on machine learning, and geophysical electromagnetic exploration and inversion.